Supplementary Information - Orbital chiral lasing in twisted bilayer metasurfaces

Mingjin Wang[1,4,5,6,*], Nianyuan Lv[2,*], Zixuan Zhang[2,*], Ye Chen[2], Jiahao Si[1], Jingxuan Chen[1], Chenyan Tang[1], Xuefan Yin[2], Zhen Liu[2], Dongxu Xin[1], Zhaozheng Yi[1], Wanhua Zheng[1,4,5,6,+], Yuri Kivshar[3,+], and Chao Peng[2,7,+]

[1]Laboratory of Solid State Optoelectronics Information Technology, Institute of Semiconductors, CAS, Beijing 100083, China

[2]State Key Laboratory of Advanced Optical Communication Systems and Networks, School of Electronics & Frontiers Science Center for Nano-optoelectronics, Peking University, Beijing 100871, China

[3]Nonlinear Physics Centre, Research School of Physics, Australian National University, Canberra ACT 2601, Australia

[4]Center of Materials Science and Optoelectronics Engineering, University of Chinese Academy of Sciences, Beijing 100049, China

[5]Hangzhou Institute for Advanced Study, University of Chinese Academy of Sciences, Hangzhou 310024, China

[6]College of Future Technology, University of Chinese Academy of Sciences, Beijing 101408, China

[7]Peng Cheng Laboratory, Shenzhen 518055, China

[*]These authors contributed equally to this work.

[+]To whom correspondence should be addressed: Wanhua Zheng (E-mail: whzheng@semi.ac.cn), Yuri Kivshar (E-mail: yuri.kivshar@anu.edu.au), Chao Peng (E-mail: pengchao@pku.edu.cn).

1 Detailed material and structure design

We begin by detailing the material composition and structural design of our InP-based twisted bilayer metasurface system. Notably, our structure features two symmetric membrane sheets made from InGaAsP multiple quantum wells (MQWs) suspended in air, with each sheet patterned by square-lattice periodic air holes defined by the lattice constant a, hole radius r, and membrane thickness h. The two sheets rotate and overlay as a twisted bilayer system, depicted by twist angle θ and gap distance g.

Each suspended membrane is composed of an upper cladding layer (246.5 nm InGaAsP), an active region (129 nm in total), and a lower cladding layer (246.5 nm InGaAsP). The active region consists of six compressively strained InGaAsP quantum wells (7.5 nm thick each) and seven lattice-matched, tensile-strained barriers (12 nm thick each). Beneath the MQWs lies a 1000 nm GaInP sacrificial layer, which is removed via wet etching to suspend the structure. The air holes are etched completely through each slab, maintaining z-axis symmetry in both layers. We design the metasurface with 50×50 air holes at a lattice constant $a = 540$ nm with the depth and radius of the circular hole being $h = 622$ nm and $r = 153$ nm, respectively. The gap distance between the upper and lower sheets is designed as $g = 100$ nm. As mentioned in the main text, the twist generates a Moiré pattern, leading to the formation of a supercell with a real-space size $L = Na$ (Fig. 1d). The twist angle θ determines the size of the supercell as $N = 1/(\sqrt{2}sin(\theta/2))$. At a twisted angle of 22.62° in our design, the supercell size of the Moiré pattern is $5/\sqrt{2}a \times 5/\sqrt{2}a$.

2 Quadratic and isotropic dispersion of Moiré supercell

When twisted metasurfaces form a Moiré lattice, the interlayer coupling alters the band dispersions. As outlined in the main text, our investigation focuses on the TE-A band near the Γ point, which exhibits fundamentally different behaviors from the reported flat-band effect in lasing, at which the coupling flattens the bands in the vicinity of the K point [1, 2]. In our design, we employ a moderately sized supercell ($5/\sqrt{2}a \times 5/\sqrt{2}a$) with a relatively large twist angle of $\theta = 22.62°$. Numerical simulations (COMSOL Multiphysics) reveal that the TE-A band in the individual layer hybridizes into two distinct modes with opposite z-symmetry, referred to as the odd and even bands (Fig. S1a). We further analyze the band dispersion near the BZ center of the Moiré supercell, which remains notably quadratic rather than flat. Additionally, the dispersion is found to be highly isotropic in reciprocal space, as evidenced by the nearly circular iso-frequency contours as shown in Fig. S1b.

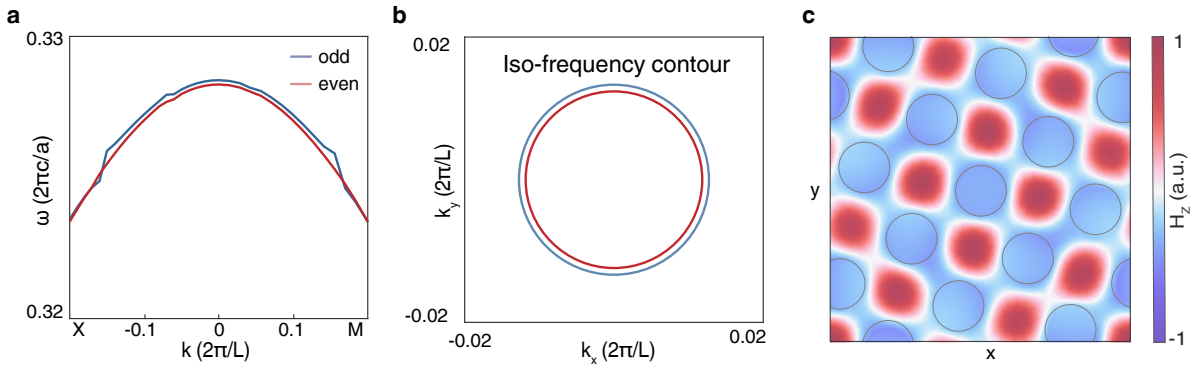

Figure 1: **The dispersion of our Moiré supercell.** (a) The band structure near the BZ center of the supercell with quadratic dispersions. (b) The corresponding iso-frequency contours, showing the dispersions are isotropic. (c) The real space H_z distribution at the supercell's BZ center.

The quadratic and isotropic dispersion of our Moiré supercell gives rise to a unique collective oscillation behavior [3]. As shown in Fig. S1c, unlike the flat-band effect [4, 5, 6, 7], the hybridized mode extends across the entire supercell rather than being confined to a few unit-cells. This delocalization occurs because the group velocity is nonzero upon the quadratic band. As a result, light can propagate through multiple supercells as “bulk guided resonances," which can further support collective guided resonances (CGRs) when confined within an effective cavity region. Second, the isotropic band dispersion reflects rotational symmetry at any angle. Combined with the circular shape of the effective cavity, the resulting CGRs modes also possess continuous rotational symmetry, rotating in either clockwise (CW) or counterclockwise (CCW) directions, respectively, showing as twofold degeneracy in a single layer.

3 Radiation suppression in Moiré lattice

To support lasing oscillation, optical modes must achieve a sufficiently high quality factor (Q). Unlike reported Moiré lattice cases where modes reside at the K point [1, 2], our mode operates at the Γ point. As a result, it naturally couples to free space and tends to radiate energy. However, this radiation loss can be suppressed through the strategic arrangement of bound states in the continuum (BICs). The simplest way is to utilize the symmetry-protected BIC at the Γ point. By decreasing the twist angle, it was reported that the Moiré mode at the BZ center gradually evolves into a near-perfect BIC, whose radiation losses are significantly reduced [8]. However, the twist angle in our design needs to be relatively large to support quadratic dispersion. In this case, the radiation loss can be almost eliminated by aligning multiple topological polarization charges across all diffraction channels, to enable robust radiation suppression across the entire Moiré band. In physics, diffraction from Moiré lattices generates multiple diffracted waves,

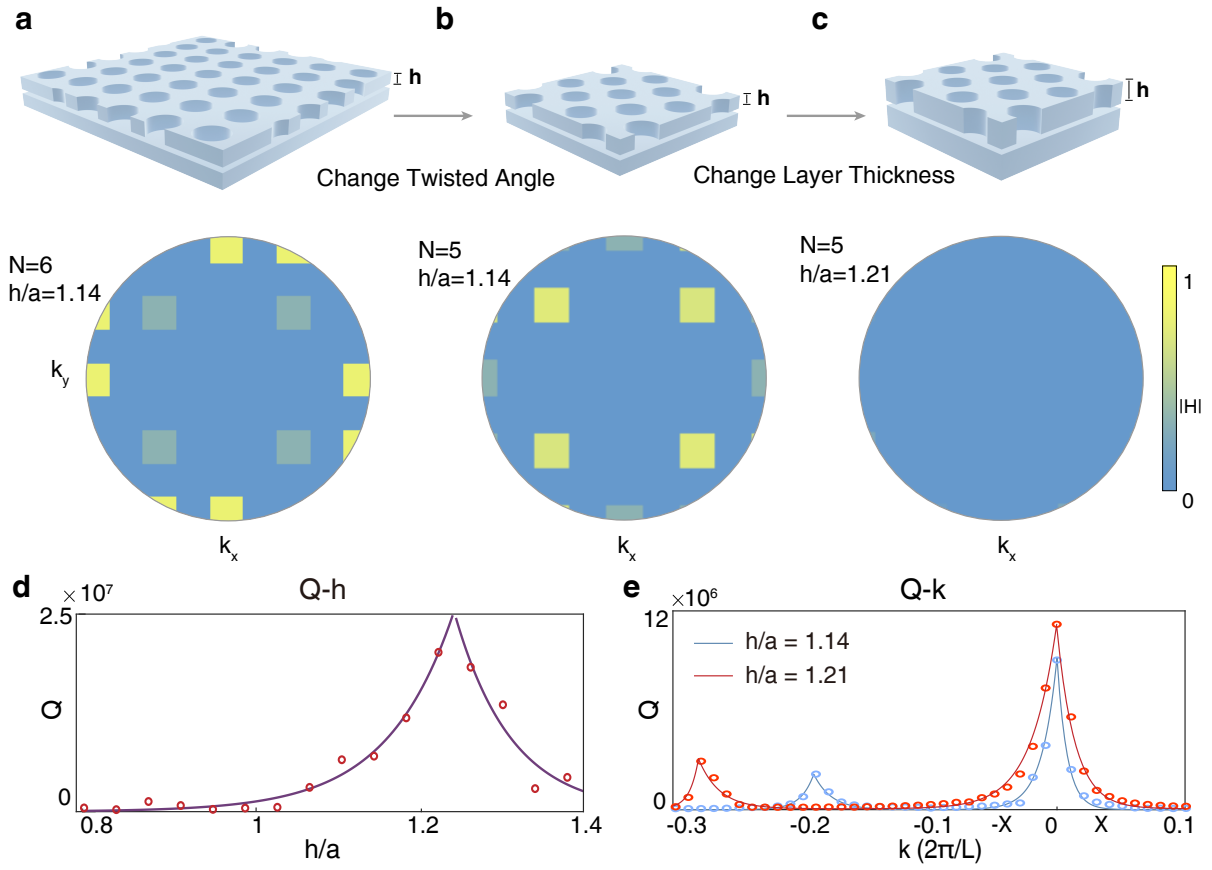

Figure 2: **Radiation suppression of Moiré lattice.** (a) For a Moiré supercell $N = 6$ and membrane thickness $h = 1.14a$ (upper panel), the radiation pattern in reciprocal space (lower panel) include multiple diffraction orders. (b) By shrinking the supercell size to $N = 5$ while keeping $h = 1.14a$ (upper panel), only a few diffraction orders remain but are still leaky (lower panel). (c) By increasing the thickness to $h = 1.21a$ while keeping $N = 5$ (upper panel), the arrangement of BICs suppresses most radiation, evidenced by a darker radiation pattern. (d) The TE-A mode's Q in a single metasurface on varying the thickness h, showing the optimal Q reaches 2.5×10^7. (e) The Qs of Moiré supercell modes in the reciprocal space, indicating the optimal design is achieved when the BICs match with the diffracted momentum.

some of which fall within the light cone (Fig. S2a). These components lead to out-of-plane energy leakage, thereby reducing the Qs of the optical modes. To suppress this radiation loss, we adopt a two-step approach in designing the geometric parameters as follows:

First, we chose a relatively large twist angle to shrink the supercell's size. Accordingly, only a few diffracted orders were left in the light cone. At $\theta = 22.62^\circ$ with $N = 5$ that compromises the quadratic and isotropic dispersion requirement mentioned above, only four diffracted orders remain radiative that are residing at the X and Y directions in the momentum space, showing as light bright spots in the far-field (Fig. S2b). Second, we apply tunable BICs to further suppress the radiation. Specifically, we fine-tune the slab thickness to $h = 1.21a$ (Fig. S2c). The BICs that carry integer topological charges evolve along the X and Y directions in the momentum space until they coincide with the diffraction orders. Combined with the symmetry-protected BIC at the BZ center, the residual radiations are effectively suppressed. As shown in the lower panel of Fig. S2c, the entire light cone becomes considerably dark.

We verified our design via numerical simulations (COMSOL Multiphysics), indicating that the Q at the supercell BZ center reaches 2.5×10^7 at $h = 1.21a$ (Fig. S2d), which is high enough to support the lasing action. The Qs of the TE-A band in the Moiré supercell are plotted in Fig. S2e for two different slab thicknesses, clearly showing the effectiveness of the BIC arrangement.

4 Laguerre-Gaussion modes in a round effective cavity

As discussed in the main text, the combination of isotropic dispersion and a rotational invariant cavity leads to twofold degenerate modes. In this section, we analytically solve the wave equation in polar coordinates and demonstrate that such modes can be described by Laguerre-Gaussian functions when a round gain-guided effective cavity is introduced.

When the twisted metasurface on the MQWs wafer is optically pumped, carrier diffusion results in a spatially non-uniform gain profile, which in turn modifies the refractive index. As an example, we consider a circular pump beam, which produces an isotropic refractive index distribution as:

$$n(\rho) = n_1(0) - n_2\rho^2 \tag{S1}$$

where ρ is the radial position, n_1 and n_2 are coefficients dependent on the material and pump power. Furthermore, due to the finite size of the incident pump spot, the variation in carrier density (and thus the change in refractive index) in the unpumped regions can be neglected. As a result, the pump spot effectively imposes a circular boundary condition on the optical mode under gain-guided operation. Substituting Eq.S1 into Maxwell's equations

$$[\frac{\partial^2}{\partial\rho^2} + \frac{1}{\rho}\frac{\partial}{\partial\rho} + \frac{1}{\rho^2}\frac{\partial^2}{\partial\phi^2} + k_0^2(\xi_0(z) - \bar{a}^2\rho^2)](\psi\rho) = \beta_0^2\psi(\rho) \tag{S2}$$

where ϕ is the azimuth angle; $\bar{a} = \sqrt{2n_1(0)n_2}/k_0 = a_r + ia_i$ is determined by the material properties. With such a refractive index profile, the finite-size modes follow slowly varying envelope approximation, in forms of Laguerre-Gaussian functions[9]:

$$\psi_{pl}(\rho,\phi) = \rho_n^{|l|}\exp(-\rho_n^2/2)L_p^{|l|}(\rho_n^2)\exp(il\phi) \tag{S3}$$

where $\rho_n = \sqrt{k_0\bar{a}}\rho$ is a dimensionless radial position, and $L_p^{|l|}(\rho^2)$ represents the generalized Laguerre polynomial with radial index p and azimuthal index l. Further, the corresponding

eigenvalues are:

$$\beta_0^2 = k_0^2 \xi_0(z) - 2k_0 \bar{a}(2p + |l| + 1) \tag{S4}$$

By comparing with the standard expression of Laguerre-Gaussian vortex beams carrying the orbital angular momentum (OAM)[10, 11]:

$$\psi_{pl}(r, \phi) = C \left(\frac{\sqrt{2} r}{w_0} \right)^{|l|} L_p^{|l|} \left(\frac{2r^2}{w_0^2} \right) \exp\left(-\frac{r^2}{w_0^2} \right) \exp\left(-il\phi \right) \tag{S5}$$

where C is a normalized constant and w_0 is the beam waist radius, we notice our solution of Eq. S3 is exactly the Laguerre-Gaussian function. Therefore, the gain-guided effective cavity indeed enables in-plane confinement, and minimizes scattering at the outer boundaries of the cavity.

The above result stems from the isotropic dispersion and geometry of our twisted metasurface system. In our device, both the gain profile, boundary conditions, and band dispersions are isotropic, obeying rotational symmetry at an arbitrary angle. Recall the fact that the bulk guided resonances that participate in the collective hybridization need to align with the isofrequency contour in momentum space. Under the omnidirectional scattering enforced by the circular boundary conditions, each component contributes with equal weighting, thus creating Laguerre-Gaussian profiles as we solved.

5 Helical and non-Hermitian couplings in twisted bilayer metasurface

The twisted metasurface's inherent chirality gives rise to a specific coupling scenario. As mentioned in the main text, we consider Laguerre-Gaussian functions $|\psi_{CW,\ CCW}^{u,\ l}\rangle$ in the upper and lower sheets as the unperturbed basis, which can rotate in CW or CCW directions. The coupling paths can be categorized into three distinct types, namely intra-layer cross-coupling ($\kappa_{1,2}^{\text{intra}}$),

inter-layer cross-coupling ($\kappa_{1,2}^{\text{inter}}$), and inter-layer direct-coupling ($\kappa_{\text{direct}}^{\text{inter}}$). Here, the terms “cross" and “direct" refer to the couplings occurring between modes with opposite or identical rotating directions, respectively. We note that all these couplings are intrinsically non-Hermitian due to the presence of radiation and material gain/loss, while the cross couplings are helical owing to the chiral nature of the twisted metasurface.

We first discuss the intralayer cross-coupling effect. As schematically illustrated in Fig. S3, we consider the modes in the lower metasurface, namely $|\psi_{CW}^{l}\rangle$ and $|\psi_{CCW}^{l}\rangle$. In this case, the upper one can be regarded as an asymmetric scatterer in real space. Seeing from the lower one, the upper metasurface breaks its mirror symmetry, meaning the system cannot be mapped onto its mirror image, so the coupling becomes directional to the helicity. Moreover, the coupling process involves radiation, absorption, and gain, rendering the coupling inherently non-Hermitian, revealing that the coupling coefficients are complex numbers. Specifically, for the lower metasurface, we describe the presence of the upper one as a perturbed Hamiltonian $\Delta\mathbf{H}$. The intralayer coupling between CW and CCW modes in the lower metasurface can be expressed as:

$$\kappa_1^{\text{intra}} = \kappa_{l,CW\to CCW}^{\text{intra}} = \langle\psi_{CCW}^{l}|\Delta H|\psi_{CW}^{l}\rangle = \int_{upper} \psi_{CCW}^{*,l}(z)\psi_{CW}^{l}(z)\Delta H(z)dz \tag{S6}$$

Here, the integral is applied to the upper membrane region where the asymmetric scatter resides, and $\psi_{CCW}^{*,l}(z)\psi_{CW}^{l}(z)$ presents the overlap in such a region. Since the $\Delta\mathbf{H}$ is non-Hermitian and helical, we got $\kappa_1^{\text{intra}} = \kappa_{l,CW\to CCW}^{\text{intra}} \neq \kappa_{l,CCW\to CW}^{\text{intra}} = \kappa_2^{\text{intra}}$.

A similar argument holds for interlayer cross-coupling. We consider the CW mode in the upper metasurface $|\psi_{CW}^{u}\rangle$ coupled with the CCW mode in the lower one $|\psi_{CCW}^{l}\rangle$ (Fig. S3), and we treat one sheet as an asymmetric scatterer to the other. The coupling coefficient can be

written as:

$$\kappa_1^{\text{inter}} = \kappa_{l,CW\to CCW}^{\text{inter}} + \kappa_{u,CW\to CCW}^{\text{inter}} = \langle\psi_{CCW}^{l}|\Delta H|\psi_{CW}^{u}\rangle + \langle\psi_{CCW}^{u}|\Delta H|\psi_{CW}^{l}\rangle$$
$$= \int_{upper} \psi_{CCW}^{*,l}(z)\psi_{CW}^{u}(z)\Delta H(z)dz + \int_{lower} \psi_{CCW}^{*,u}(z)\psi_{CW}^{l}(z)\Delta H(z)dz \tag{S7}$$

which shows that the coupling simultaneously happens at both upper and lower sheets, creating helical and non-Hermitian coupling coefficient as $\kappa_1^{\text{inter}} = \kappa_{u+l,CW\to CCW}^{\text{inter}} \neq \kappa_{u+l,CCW\to CW}^{\text{inter}} = \kappa_2^{\text{inter}}$.

The third coupling path is the direct coupling between different layers while the mode has the same helicity. We take the CW mode for example, the coupling coefficient is given by:

$$\kappa_{\text{direct}}^{\text{inter}} = \kappa_{CW\to CW}^{\text{inter}} = \langle\psi_{CW}^{u}|\Delta H|\psi_{CW}^{l}\rangle = \int_{entire} \psi_{CW}^{*,u}(z)\psi_{CW}^{l}(z)\Delta H(z)dz \tag{S8}$$

Because the compound twisted bilayer system has the same average permittivity under mirror operation, we got $\kappa_{\text{direct}}^{\text{inter}} = \kappa_{CW\to CW}^{\text{inter}} = \kappa_{CCW\to CCW}^{\text{inter}}$, showing the direct couplings are not helical but non-Hermitian.

The above discussion reveals that our twisted bilayer metasurface system is intrinsically chiral and non-Hermitian. This leads to more complex dynamics, including asymmetric coupling rates between modes and the spawn of exceptional points for chiral lasing as elaborated in the following section.

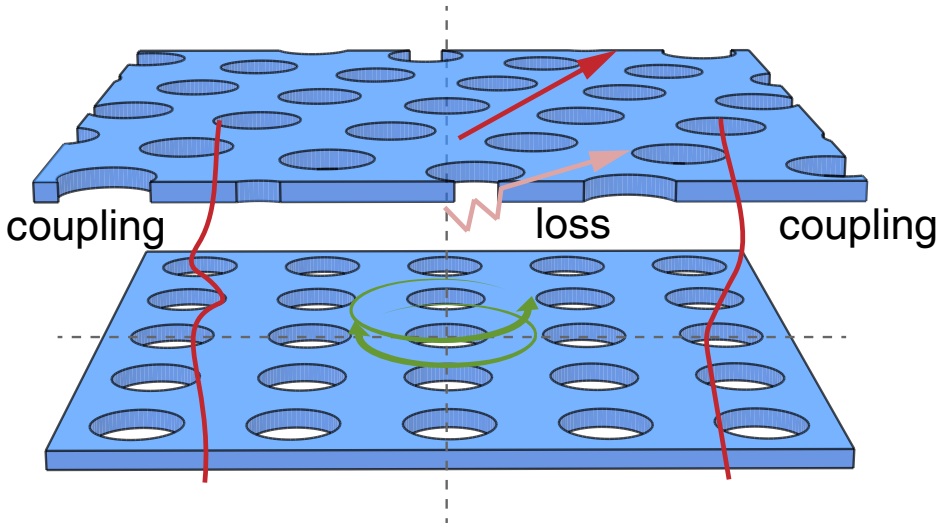

Figure 3: **Helical and non-Hermitian coupling processes in the twisted bilayer metasurfaces.** For instance, from the perspective of the lower metasurface, the upper one breaks its mirror symmetry, which makes the coupling process helical. Besides, the system possesses out-of-plane radiation and material gain/loss, so the coupling processes are generally non-Hermitian.

6 The emergence of exception points and intrinsic orbital chirality

According to the coupling paths and their strengths derived above, we write an effective Hamiltonian to depict the interplay of the four Laguerre-Gaussian functions in the upper and lower metasurfaces as the basis [12], as $\mathbf{V} = [|\psi^{u}_{CCW}\rangle,\ |\psi^{u}_{CW}\rangle,\ |\psi^{l}_{CCW}\rangle,\ |\psi^{l}_{CW}\rangle]^{T}$, which is a 4×4 coupling matrix corresponding to the following eigenvalue problem:

$$\mathbf{H}_{\text{eff}}\mathbf{V} = \begin{pmatrix} \Omega_0 & \kappa_1^{\text{intra}} & \kappa_{\text{direct}}^{\text{inter}} & \kappa_1^{\text{inter}} \\ \kappa_2^{\text{intra}} & \Omega_0 & \kappa_2^{\text{inter}} & \kappa_{\text{direct}}^{\text{inter}} \\ \kappa_{\text{direct}}^{\text{inter}} & \kappa_1^{\text{inter}} & \Omega_0 & \kappa_1^{\text{intra}} \\ \kappa_2^{\text{inter}} & \kappa_{\text{direct}}^{\text{inter}} & \kappa_2^{\text{intra}} & \Omega_0 \end{pmatrix} \mathbf{V} = \Omega'\mathbf{V} \tag{S9}$$

Here, Ω_0 is the unperturbed frequency of $|\psi^{u,\,l}_{CW,\,CCW}\rangle$; Ω' is the eigenvalue of the hybridized states through the couplings. The coupling coefficient configuration is consistent with the system's symmetry, where the upper and lower metasurfaces are identical but twisted relative to each other by a twist angle θ. By solving this eigenproblem, we get four eigenvalues as follows:

$$\Omega_1' = \Omega_0 + \kappa_{\text{direct}}^{\text{inter}} + \sqrt{(\kappa_1^{\text{intra}} + \kappa_1^{\text{inter}})(\kappa_2^{\text{intra}} + \kappa_2^{\text{inter}})} \tag{S10}$$

$$\Omega_2' = \Omega_0 + \kappa_{\text{direct}}^{\text{inter}} - \sqrt{(\kappa_1^{\text{intra}} + \kappa_1^{\text{inter}})(\kappa_2^{\text{intra}} + \kappa_2^{\text{inter}})} \tag{S11}$$

$$\Omega_3' = \Omega_0 - \kappa_{direct}^{\text{inter}} + \sqrt{(\kappa_1^{\text{intra}} - \kappa_1^{\text{inter}})(\kappa_2^{\text{intra}} - \kappa_2^{\text{inter}})} \tag{S12}$$

$$\Omega_4' = \Omega_0 - \kappa_{\text{direct}}^{\text{inter}} - \sqrt{(\kappa_1^{\text{intra}} - \kappa_1^{\text{inter}})(\kappa_2^{\text{intra}} - \kappa_2^{\text{inter}})} \tag{S13}$$

which corresponds to eigenvectors, respectively:

$$\psi_1 = \left[\quad \sqrt{\kappa_1^{\text{intra}} + \kappa_1^{\text{inter}}}, \quad \sqrt{\kappa_2^{\text{intra}} + \kappa_2^{\text{inter}}}, \quad \sqrt{\kappa_1^{\text{intra}} + \kappa_1^{\text{inter}}}, \quad \sqrt{\kappa_2^{\text{intra}} + \kappa_2^{\text{inter}}} \quad \right]^T \tag{S14}$$

$$\psi_2 = \left[-\sqrt{\kappa_1^{\text{intra}} + \kappa_1^{\text{inter}}}, \quad \sqrt{\kappa_2^{\text{intra}} + \kappa_2^{\text{inter}}}, -\sqrt{\kappa_1^{\text{intra}} + \kappa_1^{\text{inter}}}, \quad \sqrt{\kappa_2^{\text{intra}} + \kappa_2^{\text{inter}}} \quad \right]^T \tag{S15}$$

$$\psi_3 = \left[-\sqrt{\kappa_1^{\text{intra}} - \kappa_1^{\text{inter}}}, -\sqrt{\kappa_2^{\text{intra}} - \kappa_2^{\text{inter}}}, \quad \sqrt{\kappa_1^{\text{intra}} - \kappa_1^{\text{inter}}}, \quad \sqrt{\kappa_2^{\text{intra}} - \kappa_2^{\text{inter}}} \quad \right]^T \tag{S16}$$

$$\psi_4 = \left[\quad \sqrt{\kappa_1^{\text{intra}} - \kappa_1^{\text{inter}}}, -\sqrt{\kappa_2^{\text{intra}} - \kappa_2^{\text{inter}}}, -\sqrt{\kappa_1^{\text{intra}} - \kappa_1^{\text{inter}}}, \quad \sqrt{\kappa_2^{\text{intra}} - \kappa_2^{\text{inter}}} \quad \right]^T \tag{S17}$$

From the eigenvalues of the effective Hamiltonian, we found that the collapse of eigenvectors corresponding to four distinct independent conditions, namely, $\kappa_1^{\text{inter}} = \pm\kappa_1^{\text{intra}}$ or $\kappa_2^{\text{inter}} = \pm\kappa_2^{\text{intra}}$. When any one of these conditions is satisfied, two of its eigenvectors become degenerate, namely forming exceptional points (EPs). As an example, we discuss the EP at $\kappa_1^{\text{inter}} = -\kappa_1^{\text{intra}}$. At this point, the eigenvalue and eigenvector are given by

$$\Omega'_{1,2} = \Omega_0 + \kappa_{\text{direct}}^{\text{inter}} \tag{S18}$$

$$\Omega'_{3,4} = \Omega_0 - \kappa_{\text{direct}}^{\text{inter}} \pm \sqrt{2\kappa_1^{\text{intra}}(\kappa_2^{\text{intra}} - \kappa_2^{\text{inter}})} \tag{S19}$$

with

$$\psi_{1,2} = [0, 1, 0, 1]^T \tag{S20}$$

$$\psi_{3,4} = \left[\mp\sqrt{2\kappa_1^{\text{intra}}}, -\sqrt{\kappa_2^{\text{intra}} - \kappa_2^{\text{inter}}}, \pm\sqrt{2\kappa_1^{\text{intra}}}, \sqrt{\kappa_2^{\text{intra}} - \kappa_2^{\text{inter}}} \right]^T \tag{S21}$$

Such a solution reveals that the hybridized eigenmodes are divided into two branches, separated by the direct coupling strength of $\kappa_{\text{direct}}^{\text{inter}}$ as presented in Fig. 3b in the main text, while the imaginary parts of their eigen-frequencies are different due to the non-Hermitian nature of coupling. From Eq.S6-8, we found the magnitude of $\kappa_{\text{direct}}^{\text{inter}}$ is significantly larger than $\kappa_{1,2}^{\text{inter}}$ and

$\kappa_{1,2}^{\text{intra}}$ because the direct coupling counts on the average permittivity but not the perturbation of asymmetric scatter, while the former is stronger than the later one. As a result, the lower branch is more lossy, making the upper branch favorable for lasing. Fig. S4 illustrates how the system moves away from the EP by varying κ_1^{intra}, which represents the asymmetric coupling strength between the CW and CCW modes. Notably, the CW mode acquires a higher Q, rendering it more favorable for lasing.

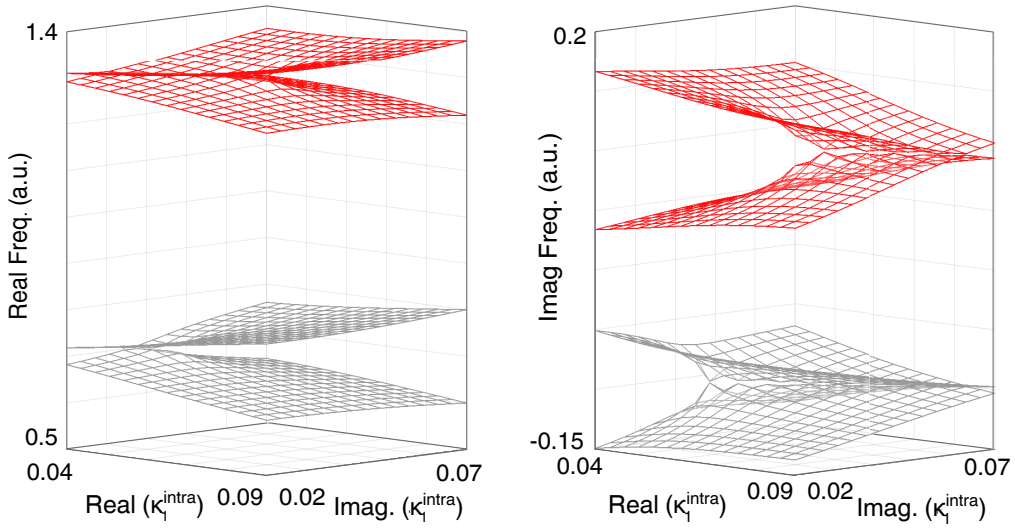

Figure 4: **Complex bands as a varying coupling coefficient κ_1^{intra}.** The real part (left) and the imaginary part (right) of the eigenfrequency.

At the EP, the two eigenmodes in the upper branch turn out to be degenerate, corresponding to the same eigenvector of $\mathbf{V} = [0, 1, 0, 1]^T$. Therefore, they represent a collective mode that rotates in a CW direction in both the upper and lower layers. We define the degree of chirality (DoC) as

$$\alpha_{ch} = \frac{|a_{CW}|^2 - |a_{CCW}|^2}{|a_{CW}|^2 + |a_{CCW}|^2} \tag{S22}$$

as the contrast between the CW and CCW components, in which α_{ch} varies from $[-1, 1]$ with ± 1 representing the pure helicity in CW or CCW directions, respectively. Thus, the above solved state exhibits the maximum degree of chirality of 1. The condition of $\kappa_1^{\text{inter}} = -\kappa_1^{\text{intra}}$ indicates a perfect balance between the interlayer and intralayer coupling strength, which is difficult to control in experiments because of the complexity of asymmetric scattering. When κ_1^{intra} deviates from the ideal EP within the shaded region in Fig. 3b in the main text, the real parts of the eigenfrequencies remain almost degenerate. However, the difference in their imaginary parts allows one mode to prevail in the mode competition, thus enabling single-mode lasing. As a supplement, we calculate the DoC near the EP region as shown in Fig. S5, showing that the lasing emission can still be considerably chiral in the non-ideal case, corresponding to observable fork patterns through self-interferences.

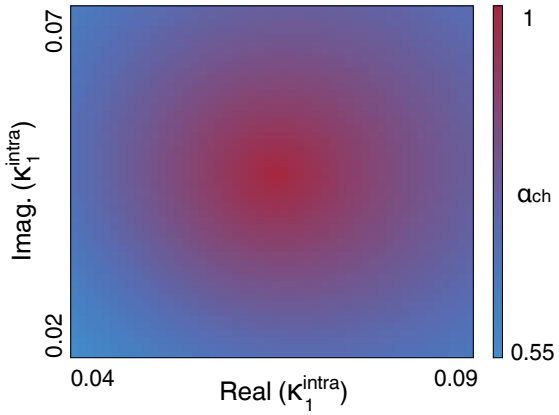

Figure 5: **The chirality near the non-Hermitian degeneracy of EP as varying κ_1^{intra}.** The degree of chirality (DoC) α_{ch} of the eigenmode.

7 Detailed measurement system for orbital chiral lasing

The detailed experimental setup is illustrated in Fig. S6, featuring a confocal microscopy system that utilizes a free-space laser as the incident light source. To ensure optimal alignment, a height-adjustable mount is placed in front of the laser, enabling precise tuning of the beam along the optical axis of the setup. The laser employed is a pulsed source operating at 1064 nm (MPL-N-1064-200uJ), with a repetition rate of 10 kHz and a pulse duration of 2 ns. For illumination, a halogen lamp is used in conjunction with a lens L_4 ($f = 150, \text{mm}$) positioned in front of it. This lens is confocal with the objective lens, providing accurate and stable illumination for sample alignment.

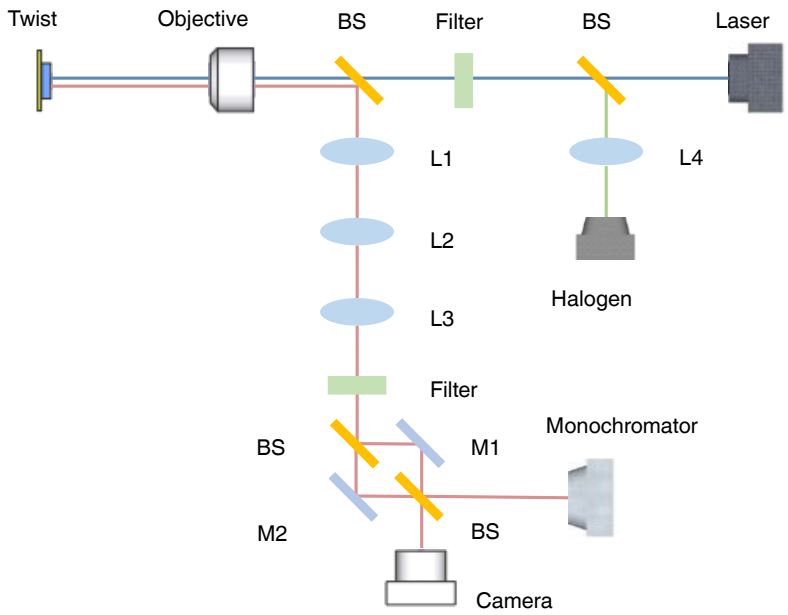

Figure 6: **The detailed experiment setup.** The illumination is performed by using the Halogen light source. The Lens parameters are given in the Method section.

8 Characterization of the gain-induced effective cavity

As discussed, the lateral light confinement in our design is achieved through a gain-induced cavity. In this section, we present experimental evidence showing that the spatial localization of the lasing mode is governed by the pump beam profile.

First, we observed that the lasing mode consistently aligns with the position of the pump beam. To verify this, we hold the pump beam fixed while translating the sample by using a motorized stage. We ensured that the pump spot remained within the metasurface region throughout the measurement. Notably, the position of the lasing mode stayed stationary despite the movement of the sample. This behavior indicates that the lasing mode is confined by the gain-induced effective cavity created by the pump beam, rather than by the physical boundaries of the metasurfaces. Detailed results are provided in the Supplementary video.

Second, we varied the pump beam's size and found that the lasing beam's size changed accordingly. As shown in Fig. S7a, we let the camera operate with fixed exposure time and gain settings to avoid automatic adjustments, which might interfere accurate measuring of beam sizes. We recorded the near-field profiles of the lasing mode after filtering out the pump light. As the pump beam expanded, the lasing mode also exhibited a corresponding increase in size. This trend was also evident in the far-field measurements. By removing lens L_2, we switched the system to a far-field configuration and observed that the far-field pattern became more focused (shrinking in angular spread) as the pump beam expanded. These results confirm that the size of the lasing mode is directly governed by the size of the incident pump beam.

Furthermore, we varied the pump energy while keeping its size and position fixed. Specifically, we opt for incident pump powers of 3.5 μW, 8 μW, and 18 μW, and the corresponding

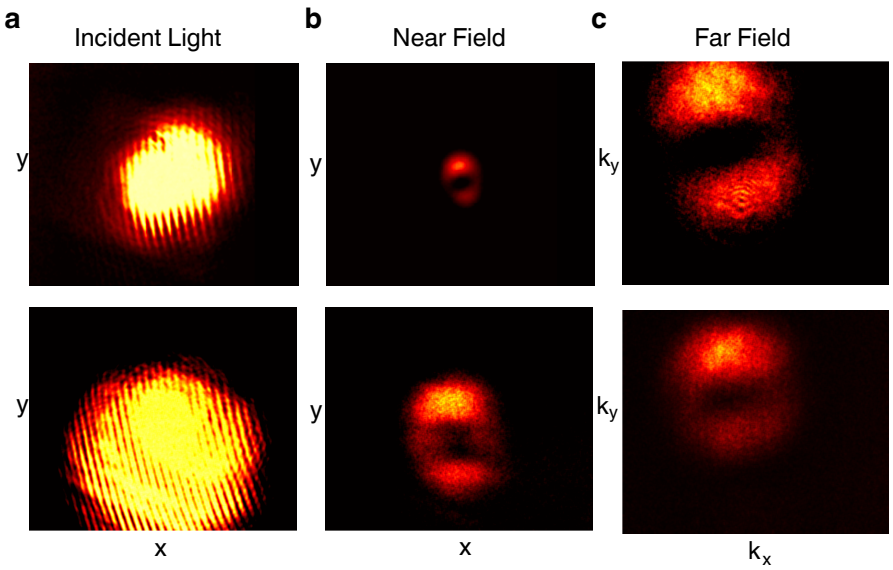

Figure 7: **Effect of changing pump beam size on the lasing beam size.** (a) The pump beam with different sizes observed from the COMS camera. (b) The near-field images of the lasing beams at different pump sizes. (c) The far-field patterns of the lasing beam at different pump sizes.

mode profiles were recorded under identical camera exposure and gain settings. As shown in Fig. S8, the lasing mode area increases slightly with higher pump power. This observation is consistent with the theoretical expectation that increased pumping enhances carrier diffusion, thereby enlarging the effective gain region available for lasing. Nevertheless, the expansion in mode size is relatively modest.

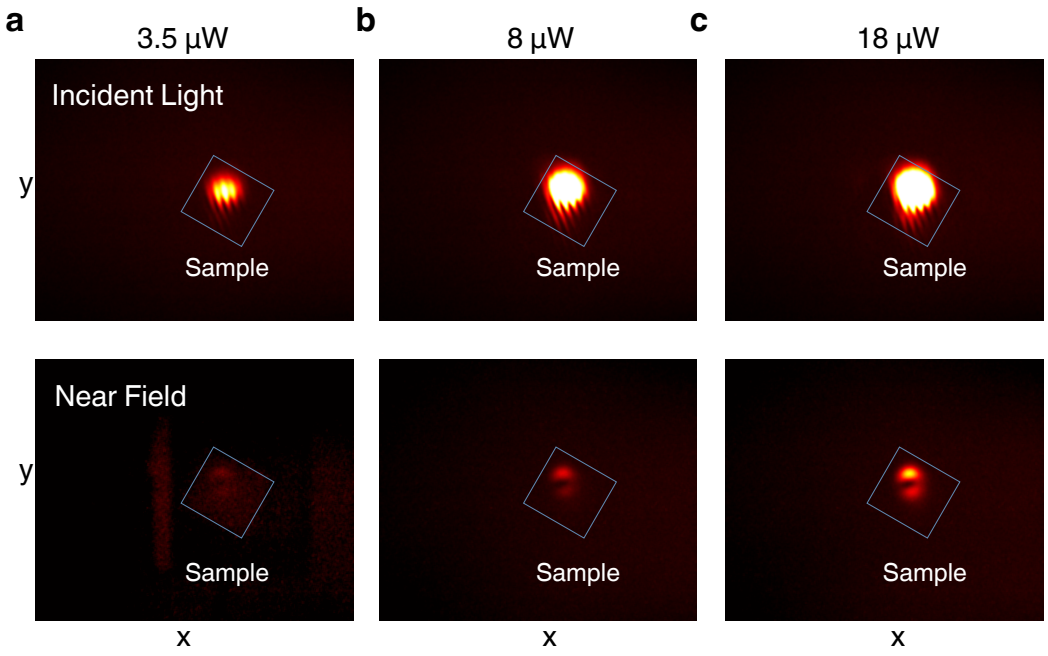

Figure 8: **Effect of changing pump beam power on the lasing beam.** The upper and lower panels show the CMOS camera images of the pump beam and lasing beam in real space, respectively. The boxes visually indicate the physical boundary of the TBPhC sample. Different pump powers are applied for (a) 3.5 μW, (b) 8 μW, and (c) 18 μW.

9 The detailed observation of the lasing process

The experimental results presented in Fig. 5 in the main text reveal that our twisted metasurface operates in a single-mode oscillation regime. As a supplement, we provide additional data to further confirm the establishment process of single-mode lasing behavior.

We begin with a low pump power of 72.5 kW/cm^2 below the lasing threshold, with its spectrum shown in Fig. S9a. At this stage, the amplified spontaneous emission (ASE) noise is prominent, nevertheless, two adjacent peaks can still be identified. These peaks correspond to the nearly degenerate eigenstates of the upper branch, as discussed in the previous section. The lower branch remains undetected due to its inherently lossy nature. This observation also suggests that our twisted metasurface system operates close to an EP condition.

As the pump power is increased to 72.8 kW/cm^2, both peaks become more pronounced and coexist (Fig. S9b), indicating that the two modes are still competing for lasing. Upon further increasing the pump power to 74 kW/cm^2, the mode competition resolves, and a single mode dominates the spectrum, as shown in Fig. S9c. This transition indicates that only the most favorable mode with a sufficient gain can surpass the lasing threshold to lase, while the competing mode is fully suppressed. During this lasing process, no external perturbation (such as asymmetric pumping we reported [13]) was applied, showing that the twisted metasurface system inherently supports mode-selection for chiral emission.

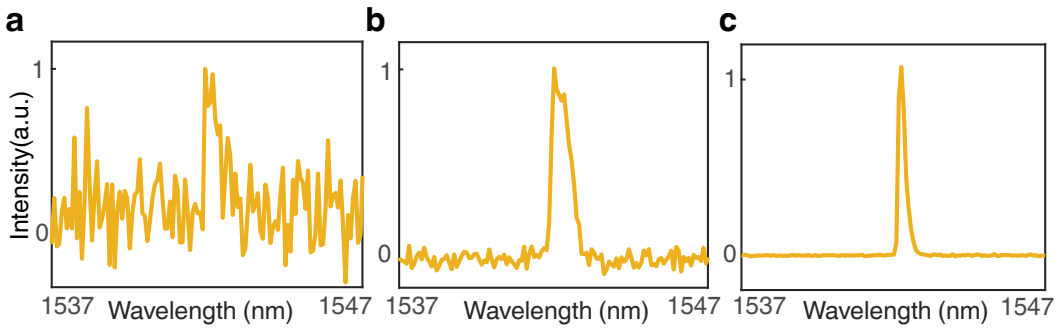

Figure 9: **The detailed lasing process through increasing the pump power** (a) Two almost degenerate modes appear on the ASE noise floor at the pump power of 72.5 kW/cm^2 which is below the lasing threhold. (b) The lasing oscillation is established at the pump power of 72.8 kW/cm^2, evidenced by significant suppression of ASE emission, but the two quasi-degenerate modes still exist. (c) The lasing transitions into single-mode lasing at the pump power of 74 kW/cm^2, only one clear lasing peak exists.

References

[1] Ma, R.-M. *et al.* Twisted lattice nanocavity with theoretical quality factor exceeding 200 billion. *Fundam. Res.* **3**, 537–543 (2023).

[2] Mao, X.-R., Shao, Z.-K., Luan, H.-Y., Wang, S.-L. & Ma, R.-M. Magic-angle lasers in nanostructured moiré superlattice. *Nat. Nanotechnol.* **16**, 1099–1105 (2021).

[3] Luan, H.-Y., Ouyang, Y.-H., Zhao, Z.-W., Mao, W.-Z. & Ma, R.-M. Reconfigurable moiré nanolaser arrays with phase synchronization. *Nature* **624**, 282–288 (2023).

[4] Luo, X.-W. & Zhang, C. Spin-twisted optical lattices: Tunable flat bands and larkin-ovchinnikov superfluids. *Phys. Rev. Lett.* **126**, 103201 (2021).

[5] Dong, K. *et al.* Flat bands in magic-angle bilayer photonic crystals at small twists. *Phys. Rev. Lett.* **126**, 223601 (2021).

[6] Wang, H., Ma, S., Zhang, S. & Lei, D. Intrinsic superflat bands in general twisted bilayer systems. *Light Sci. Appl.* **11**, 159 (2022).

[7] Yi, C.-H., Park, H. C. & Park, M. J. Strong interlayer coupling and stable topological flat bands in twisted bilayer photonic moiré superlattices. *Light Sci. Appl.* **11**, 289 (2022).

[8] Huang, L., Zhang, W. & Zhang, X. Moiré quasibound states in the continuum. *Phys. Rev. Lett.* **128**, 253901 (2022).

[9] Siegman, A. E. *Lasers* (University Science Books, 1986).

[10] Forbes, A., Mkhumbuza, L. & Feng, L. Orbital angular momentum lasers. *Nat. Rev. Phys.* **6**, 352–364 (2024).

[11] Kawase, D., Miyamoto, Y., Takeda, M., Sasaki, K. & Takeuchi, S. Observing quantum correlation of photons in laguerre-gauss modes using the gouy phase. *Phys. Rev. Lett.* **101**, 050501 (2008).

[12] Zhang, T. *et al.* Twisted moiré photonic crystal enabled optical vortex generation through bound states in the continuum. *Nat. Commun.* **14**, 6014 (2023).

[13] Chen, Y. *et al.* Chiral emission of vortex microlasers enabled by collective modes of guided resonances (2024). `2407.16499 [arXiv:physics]`.